

Parallel and Explicit Finite-Element Time-Domain Method for Maxwell Equations

Joonshik Kim and Fernando L. Teixeira, *Senior Member, IEEE*

Abstract—We construct a parallel and explicit finite-element time-domain (FETD) algorithm for Maxwell equations in simplicial meshes based on a mixed E - B discretization and a sparse approximation for the inverse mass matrix. The sparsity pattern of the approximate inverse is obtained from edge adjacency information, which is naturally encoded by the sparsity pattern of successive powers of the mass matrix. Each column of the approximate inverse is computed independently, allowing for different processors to be used with no communication costs and hence linear (ideal) speedup in parallel processors. The convergence of the approximate inverse matrix to the actual inverse (full) matrix is investigated numerically and shown to exhibit exponential convergence versus the density of the approximate inverse matrix. The resulting FETD time-stepping is explicit in the sense that it does not require a linear solve at every time step, akin to the finite-difference time-domain (FDTD) method.

Index Terms—Finite elements, FETD, differential forms, Maxwell equations, parallel computing.

I. INTRODUCTION

THE finite-element time-domain (FETD) method has been extensively used to simulate Maxwell equations in complex geometries [1], [2], [3], [4], [5], [6], [7], [8], [9], [10], [11]. FETD in simplicial meshes typically requires a linear solve at every time-step. This is a basic drawback of the method, and is in contrast to, for example, the finite-difference time-domain (FDTD) method in rectangular meshes, which is a “matrix-free” algorithm [12].

In [7], the construction of an “explicit” FETD time-stepping (“marching-on-time”) algorithm, i.e. with no need for a linear solve at every time step, was proposed in irregular meshes. This explicit FETD based on a FE discretization with mixed basis functions [3], [13] (denoted as “mixed E - B FETD” [9], [10]) and a SPAI (SParse Approximated Inverse) algorithm [14] to obtain a sparse approximate inverse mass (Hodge) matrix.

In this work, we construct a parallel version of the SPAI-based, explicit FETD scheme in simplicial meshes and analyze its performance in three-dimensional (3-D) simulations of Maxwell equations. A key step in the proposed SPAI approximation is the a priori setup of a sparsity pattern for the approximate inverse. Here, we employ sparsity patterns given by successive powers of the mass matrix, which describe successive high-level adjacencies between the edges of the

mesh. We examine the convergence of the approximate system matrix inverse (in general, a combination of mass and stiffness matrices) and of the approximate mass matrix inverse to their respective exact inverses (which are full), for different sparsity levels and time step increments. We show that exponential convergence is obtained for time scales below the Courant limit, where the system matrix converges to the mass matrix. We discuss how this exponential convergence is associated with properties of the Hodge star operator, which is the continuum equivalent to the mass matrix. Because no communication cost between processors is incurred in the computation of sparse approximate inverses, linear (ideal) speed up can be achieved in parallel processor systems.

II. DISCRETIZATION

A. Mixed E - B FETD

We write Maxwell equations as [15], [16], [18]

$$dE = -\frac{\partial}{\partial t}B \quad (1)$$

$$d\star_{\mu-1}B = \frac{\partial}{\partial t}\star_{\epsilon}E \quad (2)$$

where E is a 1-form, B is a 2-form, and d is the exterior derivative operator. The Hodge star (or simply Hodge) operators \star_{ϵ} and $\star_{\mu-1}$ generalize the constitutive relations to incorporate all metric information as well [19], [20], [21], [22], [23], [24], [25]. The discretization of the above is done by expanding E and B in terms on Whitney forms [16], [17]. By denoting the Whitney p -form associated with the i -th p -cell (viz., nodes, edges, faces, volumes for $p = 0, 1, 2, 3$ respectively) as W_i^p , the expansion writes [7], [9]

$$E = \sum_{i=1}^{N_e} e_i W_i^1 \quad (3)$$

$$B = \sum_{i=1}^{N_f} b_i W_i^2 \quad (4)$$

where N_e , N_f are the total number of edges and faces of the 3-D FE mesh, respectively. The semi-discrete counterpart to (1) and (2) is [7], [9], [10], [13]

$$\mathbf{C}e = -\frac{d}{dt}\mathbf{b} \quad (5)$$

$$\mathbf{C}^T[\star_{\mu-1}^{-1}]\mathbf{b} = \frac{d}{dt}[\star_{\epsilon}]e \quad (6)$$

where

$$\mathbf{e} = [e_1, \dots, e_{N_e}]^T \quad (7)$$

$$\mathbf{b} = [b_1, \dots, b_{N_f}]^T \quad (8)$$

$$(9)$$

Manuscript received MM,DD,YYYY.

The authors are with the ElectroScience Laboratory and the Department of Electrical and Computer Engineering, 1320 Kinnear Road, The Ohio State University, Columbus, Ohio, 43212, USA. This work was supported in part by NSF grants ECCS-0347502 and ECCS-0925272, and AFOSR grant FA 9550-04-1-0359. Supercomputing resources were provided by the Ohio Supercomputing Center under grants PAS-0061 and PAS-0110.

are the arrays of degrees of freedom (unknowns), \mathbf{C} is the incidence matrix (or, less generically, the curl matrix) representing the discrete exterior derivative acting on 1-forms (see, e.g. [23]), and the discrete Hodge matrices $[\star_\epsilon]$, $[\star_\mu^{-1}]$ are symmetric positive-definite matrices given by the volume integrals [7], [22]

$$[\star_\epsilon]_{ij} = \int_{\Omega} \epsilon W_i^1 \wedge \star W_j^1 \quad (10)$$

$$[\star_\mu^{-1}]_{ij} = \int_{\Omega} \frac{1}{\mu} W_i^2 \wedge \star W_j^2 \quad (11)$$

where \wedge is the wedge (exterior) product and Ω represents the integrand support. The matrix \mathbf{C} depends only on the mesh connectivity, i.e., it has a purely “topological” character, with elements assuming values in $\{-1, 0, 1\}$ only [18], [23], [26].

By approximating the time derivatives by staggered central-differences, the following leap-frog time update scheme results [9], [13]

$$\mathbf{b}_n = \mathbf{b}_{n-1} - \Delta t \mathbf{C} \mathbf{e}_{n-\frac{1}{2}} \quad (12)$$

$$[\star_\epsilon] \mathbf{e}_{n+\frac{1}{2}} = [\star_\epsilon] \mathbf{e}_{n-\frac{1}{2}} + \Delta t \mathbf{C}^T [\star_\mu^{-1}] \mathbf{b}_n. \quad (13)$$

where n is the discrete time index. This is a conditionally stable update where the maximum time step Δt is found by requiring the eigenvalues of the associated system matrix (or the root loci of the associated z transform) to be within the unit circle of the complex plane. This leads to the stability condition [27], [28]

$$\Delta t \leq \frac{2}{\sqrt{\max(\lambda_{\mathbf{X}})}} \quad (14)$$

where $\lambda_{\mathbf{X}}$ is the eigenvalue set of the matrix

$$\mathbf{X} = [\star_\epsilon]^{-1} \mathbf{C}^T [\star_\mu^{-1}] \mathbf{C}. \quad (15)$$

B. Vector-Wave-Equation FETD

The discretization described in the previous section uses both electric and magnetic fields as unknown and expands them using a mixed set of basis functions. More traditionally, FETD discretizations have been done using the second-order vector wave equation in terms of the electric field vector \vec{E} , that is

$$\nabla \times \left\{ \frac{1}{\mu} \nabla \times \vec{E} \right\} + \epsilon \frac{\partial^2}{\partial t^2} \vec{E} = 0 \quad (16)$$

followed by a projection of the electric field onto a discrete vector space spanned by (vector) edge elements \vec{W}_i^1 (proxies of Whitney 1-forms W_i^1 [16]) as

$$\vec{E} = \sum_{i=1}^{N_e} e_i \vec{W}_i^1 \quad (17)$$

and by Galerkin’s testing [2], [29] to give the semi-discrete equations

$$\mathbf{M} \frac{d^2}{dt^2} \mathbf{e} + \mathbf{S} \mathbf{e} = 0 \quad (18)$$

where \mathbf{e} is the same vector as in (7) and the elements of the mass matrix \mathbf{M} and the stiffness matrix \mathbf{S} are given by the

volume integrals

$$\mathbf{M}_{ij} = \int_{\Omega} \epsilon W_i^1 \wedge \star W_j^1 \quad (19)$$

$$\mathbf{S}_{ij} = \int_{\Omega} \frac{1}{\mu} dW_i^1 \wedge \star dW_j^1 \quad (20)$$

which can be expressed alternatively as

$$\mathbf{M}_{ij} = \int_{\Omega} \epsilon \vec{W}_i^1 \cdot \vec{W}_j^1 dV \quad (21)$$

$$\mathbf{S}_{ij} = \int_{\Omega} \frac{1}{\mu} (\nabla \times \vec{W}_i^1) \cdot (\nabla \times \vec{W}_j^1) dV \quad (22)$$

where dV is a volume element. Note that $\mathbf{M} = [\star_\epsilon]$.

There are various consistent ways to perform the time discretization of the above. Backward- and central-differences are among the simplest choices [2]. The resulting time updates are respectively written as

$$(\mathbf{M} + \Delta t^2 \mathbf{S}) \mathbf{e}_{n+1} = 2\mathbf{M} \mathbf{e}_n - \mathbf{M} \mathbf{e}_{n-1}, \quad (23)$$

and

$$\mathbf{M} \mathbf{e}_{n+1} = (2\mathbf{M} - \Delta t^2 \mathbf{S}) \mathbf{e}_n - \mathbf{M} \mathbf{e}_{n-1}. \quad (24)$$

The update scheme (23) is unconditionally stable, whereas update (24) is conditionally stable with maximum time step given by [2]

$$\Delta t \leq \frac{2}{\sqrt{\max(\lambda_{\mathbf{X}})}} \quad (25)$$

where $\lambda_{\mathbf{X}}$ is the set of eigenvalues of the matrix

$$\mathbf{X} = \mathbf{M}^{-1} \mathbf{S}. \quad (26)$$

This stability condition is equivalent to that of (14) because $\mathbf{S} = \mathbf{C}^T [\star_\mu^{-1}] \mathbf{C}$, see [22] for example. Note also that by eliminating the magnetic field in (5) and (6), we get the semi-discrete wave equation

$$[\star_\epsilon] \frac{d^2}{dt^2} \mathbf{e} + \mathbf{C}^T [\star_\mu^{-1}] \mathbf{C} \mathbf{e} = 0 \quad (27)$$

which is equivalent to (18).

III. EXPLICIT AND PARALLEL FETD

The time stepping schemes described in the previous Section require a linear solve *at every time step* in simplicial meshes. This is a major computational bottleneck and, hence, it is highly desirable to develop *explicit* updates, where no linear solve is necessary during time-stepping.

The most “direct” way to produce an explicit FETD update, starting from (12) and (13), would be to simply write

$$\mathbf{b}_n = \mathbf{b}_{n-1} - \Delta t \mathbf{C} \mathbf{e}_{n-\frac{1}{2}} \quad (28)$$

$$\mathbf{e}_{n+\frac{1}{2}} = \mathbf{e}_{n-\frac{1}{2}} + \Delta t [\star_\epsilon]^{-1} \mathbf{C}^T [\star_\mu^{-1}] \mathbf{b}_n. \quad (29)$$

where $[\star_\epsilon]^{-1}$ is obtained numerically. This is of course wholly impractical for large problems not only because the computational cost of obtaining $[\star_\epsilon]^{-1}$ is too high, but also because $[\star_\epsilon]^{-1}$ is in general a full matrix.

Reference [13] discusses the use of a sparse approximation for $[\star_\epsilon]^{-1}$ as a route to derive an explicit FETD. Here, we describe an embarrassingly parallel algorithm to compute

the sparse approximation, and show an implementation the resulting algorithm in simplicial meshes. We explain the convergence results obtained in view of the Hodge star operator properties.

A. Parallel Computation of Approximate $[\star_\epsilon]^{-1}$

Consider the generic linear system

$$\mathbf{A}\mathbf{x} = \mathbf{b} \quad (30)$$

The SPAI algorithm approximates the sparse inverse $\hat{\mathbf{A}}^{-1}$ by minimizing Frobenius norm $\|\cdot\|_F$ of the error matrix $\mathbf{E}_r = \mathbf{A}\hat{\mathbf{A}}^{-1} - \mathbf{I}$, and it is implemented here as follows:

- 1) Prepare the sparsity pattern \mathbf{P} of the approximated inverse matrix. This step will be discussed in more detail in the next section below.
- 2) Select the k -th column of \mathbf{P} , denoted as \mathbf{m}_k and the k -th column of the identity matrix, denoted as \mathbf{e}_k .
- 3) Build a column index vector \mathcal{J} from the indices j such that $m_k(j) \neq 0$.
- 4) Build a row index vector \mathcal{I} such that it removes the zero rows of $\mathbf{A}(i, \mathcal{J})$.
- 5) Prepare a submatrix $\mathbf{A}(\mathcal{I}, \mathcal{J}) = \bar{\mathbf{A}}$.
- 6) Prepare subvectors $\bar{\mathbf{e}}_k = \mathbf{e}_k(\mathcal{I})$ and $\bar{\mathbf{m}}_k = \mathbf{m}_k(\mathcal{J})$.
- 7) Find $\bar{\mathbf{m}}_k$ that minimize $\|\bar{\mathbf{A}}\bar{\mathbf{m}}_k - \bar{\mathbf{e}}_k\|_2$. This can be done by a least square method to solve an over determined system equation. $\bar{\mathbf{A}}\bar{\mathbf{m}}_k - \bar{\mathbf{e}}_k$.
- 8) Insert calculated $\bar{\mathbf{m}}_k$ into original column \mathbf{m}_k of \mathbf{P} by $\mathbf{m}_k(\mathcal{J}) = \bar{\mathbf{m}}_k$.
- 9) By repeating the above procedure for all columns k , \mathbf{P} becomes the approximate inverse $\hat{\mathbf{A}}^{-1}$ sought.

This above procedure is embarrassingly parallel because it is done for each k column column independently. The resulting FETD update writes

$$\mathbf{b}_n = \mathbf{b}_{n-1} - \Delta t \mathbf{C} \mathbf{e}_{n-\frac{1}{2}} \quad (31)$$

$$\mathbf{e}_{n+\frac{1}{2}} = \mathbf{e}_{n-\frac{1}{2}} + \Delta t [\star_\epsilon]^{-1} \mathbf{C}^T [\star_\mu^{-1}] \mathbf{b}_n. \quad (32)$$

where $[\star_\epsilon]^{-1}$ is the sparse approximation of $[\star_\epsilon]^{-1}$, obtained as above. Since both (31) and (32) involve spatial stencils of limited span, this time-stepping procedure itself can also be parallelizable, similarly to high-order FDTD algorithms having extended spatial stencils. Note that the above computation for $[\star_\epsilon]^{-1}$ may lead to a slightly asymmetric matrix due to numeric round-off error. Symmetry can be enforced a posteriori by letting $[\star_\epsilon]^{-1} \rightarrow 1/2([\star_\epsilon]^{-1} + [\star_\epsilon]^{-T})$, where $[\star_\epsilon]^{-T}$ is the transpose of $[\star_\epsilon]^{-1}$. Enforcing exact symmetry in $[\star_\epsilon]^{-1}$ is important for the stability of the resulting FETD algorithm [27].

B. Sparsity Pattern Computation

The SPAI algorithm above requires the sparsity pattern of the approximate inverse to be determined a priori. A simple approach to construct such sparsity pattern using mesh connectivity information based on powers of the mass matrix was suggested in [7] and further discussed in [13]. An equivalent approach was also considered in detail in [30]. As seen from (21), the sparsity pattern of the Hodge matrix $[\star_\epsilon] =$

\mathbf{M} encodes information about the nearest-neighbor adjacency between edges in the FE mesh. Moreover, sparsity patterns of Hodge matrix powers \mathbf{M}^k , $k = 1, 2, \dots$ encode successively high-level adjacencies between edges. It is reasonable to choose these very sparsity patterns for the approximate inverse Hodge matrix because not only \star_ϵ but also \star_ϵ^{-1} are strictly local operators in the continuum. As k increases, we trade the sparsity for accuracy in the computation of the approximate inverse, as illustrated in the following section.

C. Convergence of the Sparse Approximate Inverse

Fig. 1 illustrates the convergence of the sparse approximate inverse (using sparsity patterns of \mathbf{M}^k , $k = 1, \dots, 4$) to the true inverse by measuring Frobenius norm of the error matrix \mathbf{E}_r defined before, with

$$\mathbf{A} = \mathbf{M} + \Delta t^2 \mathbf{S}, \quad (33)$$

which is the linear system matrix in (23) and, for $\Delta t = 0$, recovers the linear system matrix $\mathbf{M} = [\star_\epsilon]$ in (13) and (24). The three-dimensional finite element mesh used to generate Fig. 1 results has a total of 643 edges and is shown in Fig. 2. It discretizes a rectangular domain of size $3 \times 4 \times 5$ m³ with Dirichlet boundary conditions (for the electric field). From Fig. 1 we observe that the sparse approximate inverse converges very quickly to the true inverse for small Δt as k increases. In particular, the convergence is exponential when $\Delta t = 0$ in (33), which is the case of primary interest here for when the system matrix in the explicit update (13) is recovered.

The Courant limit given by (14) (and equal to 0.673783 ns in this example) is also indicated in Fig. 1. This limit of course does not apply to (23), which is an unconditionally stable update. It simply serves to indicate here how small the time step should be vis-à-vis the average mesh size to obtain exponential convergence, and also that this remains roughly invariant with mesh size, provided the mesh is as uniform as possible. Because the time step size for exponential convergence is much smaller than the Courant limit, it follows the use of such sparse approximate inverse is less suited for an implicit scheme such as (23). This can be explained by comparing (16) and (18): the matrix $\mathbf{S} + \frac{1}{\Delta t^2} \mathbf{M}$ corresponds to a discrete version of the differential operator $\nabla \times \frac{1}{\mu} \nabla \times + \epsilon \frac{\partial^2}{\partial t^2}$. The inverse of the latter (Green's function) exhibits a long-range, $1/r$ algebraic decay (as opposed to \star_ϵ^{-1} , which is strictly local as noted before)¹.

D. Parallel Speedup

The speedup provided by parallelization is shown in Fig. 3. The graph indicates the reciprocal time for constructing the approximated inverse of a 205,920² mass matrix with $k = 3$, versus the number of processors in the cluster. The cluster employed in this result is made of identical dual-socket, dual-core 2.6 GHz AMD Opteron processors with 8 GB RAM

¹In this case, other sparsity patterns relying, for example, on heuristics about the underlying Green's function may be better suited to provide approximate inverses. These would be inevitably less precise though, and primarily applicable only as preconditioners [14], [31], [32].

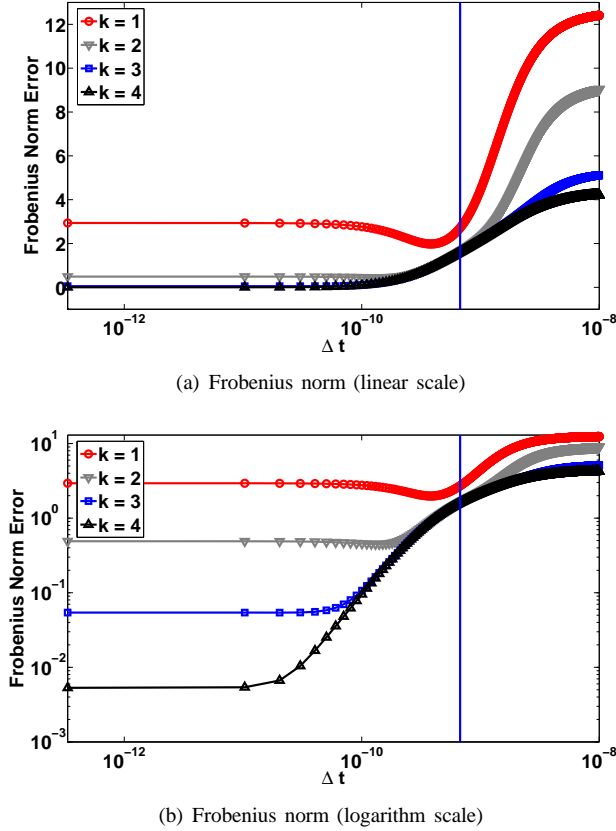


Fig. 1. Linear-scale and log-scale plots of $\|\mathbf{A}\hat{\mathbf{A}}^{-1} - \mathbf{I}\|_F$, for $\mathbf{A} = \mathbf{M} + \Delta t^2 \mathbf{S}$. Note that for $\Delta t \rightarrow 0$ (left region), the system matrix \mathbf{A} converges to the mass matrix. In this regime, the convergence of the matrix norm $\|\mathbf{A}\hat{\mathbf{A}}^{-1} - \mathbf{I}\|_F$ is exponential with increasing k , as clearly seen from the logarithm scale plot. The vertical line indicates the Courant stability limit (14) for Δt .

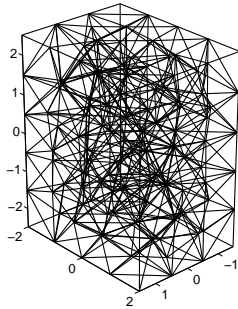


Fig. 2. Finite element mesh of a $3 \times 4 \times 5 \text{ m}^3$ rectangular domain used for the convergence study in Fig. 1.

each. We can see that the reciprocal time increases linearly (ideal speedup) as we add more processors in the the cluster, as there is no need for the processors to communicate with each other during the approximate inverse computation.

E. Eigenmode Convergence Analysis

We next study the convergence of the field solution by first considering the dominant eigenmode solution in a two-dimensional rectangular cavity with perfectly conducting

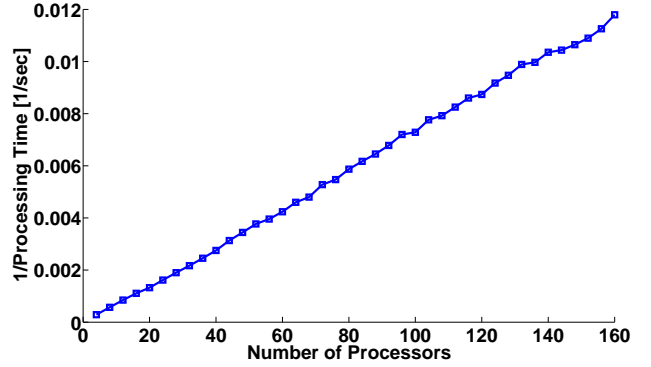


Fig. 3. Reciprocal of the processing time to obtain the approximate inverse of the Hodge matrix as a function of the number of processors. In this example, the Hodge matrix considered has $205,920^2$ elements and $k = 3$. The speedup observed is linear (ideal) because the processors do not need to communicate with each other.

(PEC) walls. We examine the accuracy of the results for different mesh refinements and parameters k . This is a simple geometry that admits exact solutions, which can be used as reference. The solution for the dominant mode is obtained directly from the associated eigenvector of the finite element system matrix. In other words, a time-stepping is not utilized in this case. Furthermore, as there is no geometrical error stemming from a discrete rendering of the cavity, the errors due to the sparse approximate inversion of $[\star_\epsilon]$ and the *spatial* discretization of the field can be better isolated.

We first compute the sparse-approximate-inverse error or “*i*-error”, on the electric field for various k and mesh refinements. Note that dominant eigenmode distribution, TE_{10} , depends solely on the aspect ratio of this cavity, which is chosen as 0.9. The *i*-error is computed assuming as reference the solution employing the direct (numerically exact, full matrix) inverse, that is

$$\iint_S \frac{\|\vec{E}^s - \vec{E}^d\|^2}{\|\vec{E}^d\|^2} dx dy \quad (34)$$

where \vec{E}^s is the finite element solution using sparse approximate inverse $[\star_\epsilon]^{-1}$, and \vec{E}^d is the finite element solution using exact inverse $[\star_\epsilon]^{-1}$.

Fig. 4 shows the convergence of the *i*-error for various values of k and different mesh refinements. Five irregular simplicial meshes are considered, with $d = 8h, 16h, 32h, 64h$, and $128h$, where d is the shortest side of the cavity and h is the average edge length of the mesh elements. We observe an exponential convergence of the results with increasing k , in agreement with Fig. 1 in the $\Delta t \rightarrow 0$ limit. Table I lists the numerical values of the corresponding *i*-errors.

We next compute the discretization error, or “*(i + s)*-error”. This is the error computed by using the analytical solution as reference, that is

$$\iint_S \frac{\|\vec{E}^s - \vec{E}^a\|^2}{\|\vec{E}^a\|^2} dx dy \quad (35)$$

where \vec{E}^a represents the exact TE_{10} eigenmode of the rectangular cavity. The *(i + s)*-error includes the error caused

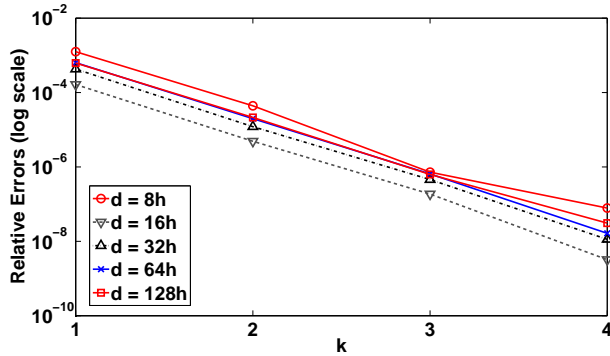


Fig. 4. Plot of the i -error on the (dominant mode) electric field for various k , showing exponential convergence irrespective of the mesh resolution.

TABLE I
 i -ERROR ON DOMINANT EIGENMODE

d	$k = 1$	$k = 2$	$k = 3$	$k = 4$
8h	0.0012541424	0.0000439891	0.0000007233	0.0000000784
16h	0.0001642943	0.0000048964	0.0000001870	0.0000000032
32h	0.0004281827	0.0000120741	0.0000004573	0.0000000113
64h	0.0006355718	0.0000198796	0.0000006479	0.0000000164
128h	0.0006213499	0.0000213711	0.0000006286	0.0000000309

by approximate inverse computation of $[\star_\epsilon]^{-1}$ and the error caused by the (spatial) finite element discretization itself.

Fig. 5 plots the $(i + s)$ -error under various k and different mesh refinements, for the same five simplicial meshes as before. Note that due to the exponential convergence of the approximate inverse, the error caused by the spatial discretization quickly dominates the $(i + s)$ -error as k is increased. In particular, $k = 3$ is sufficient for all h considered. Table II lists the corresponding numerical values.

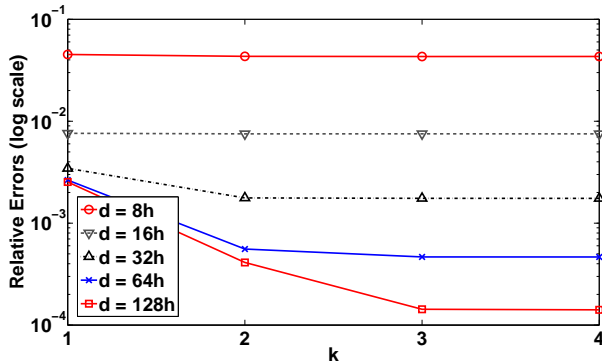


Fig. 5. Plot of the $(i + s)$ -error on the (dominant mode) electric field for various k and mesh refinements. Note that $k = 3$ suffice for all resolutions considered (i.e., $k = 4$ does not reduce the total error further).

Next, we consider a three-dimensional cavity example with time-stepping. Note that the FETD update (31) and (32) has a truncation error of second order, Δt^2 , and a cumulative numerical dispersion error. We excite the electric field using a spatially-uncorrelated random field distribution (white noise) at $t = 0$ and examine the cavity spectrum by taking the FFT of the computed FETD time-domain data. The settings of the FETD simulation are as follows. The size of prepared PEC

TABLE II
 $(i + s)$ -ERROR ON DOMINANT EIGENMODE

d	$k = 1$	$k = 2$	$k = 3$	$k = 4$
8h	0.0451671408	0.0433014775	0.0431448067	0.0431737723
16h	0.0076124376	0.0075139275	0.0075237090	0.0075209606
32h	0.0034503909	0.0017692151	0.0017521090	0.0017515103
64h	0.0026455523	0.0005574514	0.0004663317	0.0004656869
128h	0.0025342864	0.0004113815	0.0001429546	0.0001412352

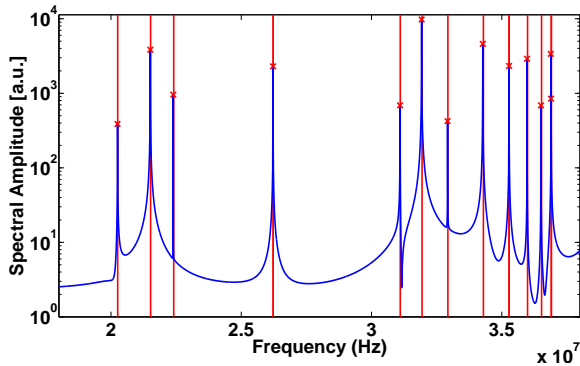
cavity is $9 \times 10 \times 11$ m. The simplicial (tetrahedral) mesh has $d = 64h$, where d again refers to the shortest side of the cavity and h to the average length of the mesh element edges. The corresponding incidence matrix $[\mathbf{C}]$ has $433,798 \times 259,580$ elements (this is also an indicator of the mesh size, as the number of rows and columns in $[\mathbf{C}]$ corresponds to number of facets and edges of the mesh, respectively). For this mesh, the ratio of fill-ins of $[\star_\epsilon]^{-1}$ relative to the fill-ins of $[\star_\epsilon]$ for $k = 0, 1, 2, 3, 4$ are equal to 0.0627, 1.00, 5.40, 17.19, 39.96, respectively (these numbers are close to what should be expected for three-dimensional simplicial meshes in general).

The FETD results below employs $k = 3$. The time increment Δt is such that $c\Delta t = 0.0625$ m, where c is the speed of light in m/s. The frequency resolution of the FFT is sufficiently fine not to perturb the underlying accuracy of the finite element discretization. To guarantee a given spectral resolution of Δf , we have $N\Delta t \geq 1/\Delta f$, where N is the total number of time steps (FFT samples) [11]. The simulation employs $N = 16 \times 10^6$, yielding $\Delta f = 1 \times 10^{-6}c$ Hz. This large N (and fine spectral resolution) is beyond what is necessary in most applications, but it serves to also verify the late-time stability of the proposed FETD algorithm.

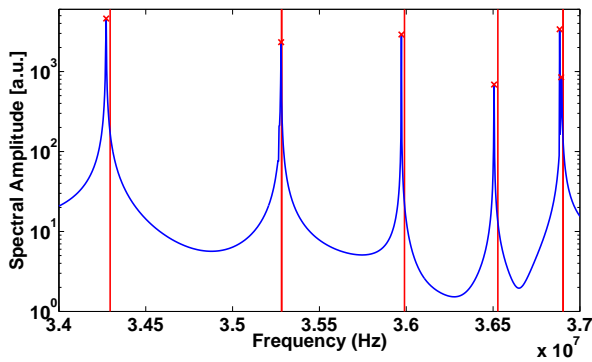
Fig. 6 depicts the spectral amplitude of the cavity field computed by FETD using (28)–(29). Fig. 6(a) shows the spectrum in a frequency range that includes the thirteen lowest eigenfrequencies. The vertical red lines indicate the exact eigenvalues. Excellent agreement is obtained between the computed and exact eigenvalues. Fig. 6(b) shows a zoomed view of the spectrum around the frequency range 34–37 GHz. The splitting of two degenerate eigenfrequencies near 37 GHz is visible in this plot. This splitting is caused by the irregular mesh discretization, which slightly perturbs the symmetry of corresponding eigenmodes.

IV. CONCLUSION

We have discussed a parallel and explicit (with leap-frog time-stepping) FETD algorithm that utilizes a sparse approximation of the inverse of the Hodge (mass) matrix. The sparsity pattern of the approximate inverse is pre-computed using powers of the Hodge matrix itself, which encode edge adjacency information of the mesh. The sparse approximate inverse matrix computation is performed independently for each column and in a parallel way with no communication costs, and hence ideal (linear) speed-up with the number of processors. The approximate inverse of the Hodge matrix is shown to converge exponentially to the true (full) inverse with increasing number of adjacency levels k (fill-in factor).



(a) Spectral amplitude of the cavity field computed by FETD. The eigenfrequencies f_a^i are extracted from the spectral peaks and indicated by the crosses. The vertical lines represent the exact eigenfrequencies f_e^i , for $i = 1, 2, \dots, 13$.



(b) Zoomed view of the 34–37 GHz frequency window, showing the splitting of the degenerate eigenfrequencies near 37 GHz caused by discretization.

Fig. 6. Spectral amplitude of the electromagnetic field inside a three-dimensional cavity computed by FETD using (28)–(29) with $k = 3$.

The exponential convergence is explained by invoking the (strictly) local nature of the inverse Hodge star operator (in the continuum limit). Numerical results involving two- and three-dimensional problems have illustrated the efficacy of the proposed algorithm.

REFERENCES

- [1] J.-F. Lee, R. Lee, and A. C. Cangellaris, "Time domain finite element methods," *IEEE Trans. Antennas Propagat.*, vol. 45, no. 3, pp. 430–442, 1997.
- [2] J. Jin, *The Finite Element Method in Electromagnetics*, Second Edition, Wiley, New York, 2002.
- [3] M.F. Wong, O. Picon, V.F. Hanna, "A finite element method based on Whitney forms to solve Maxwell equations in the time domain," *IEEE Trans. Magn.*, vol. 31, no. 3, May 1995.
- [4] M. Feliziani and F. Maradei, "Hybrid finite element solution of time dependent Maxwell's curl equations," *IEEE Trans. Magn.*, vol. 31, no. 3, pp. 1330–1335, May 1995.
- [5] T. V. Yioultis, N. V. Kantartzis, C. S. Antonopoulos, and T. D. Tsiboukis, "A fully explicit Whitney-element time-domain scheme with higher order vector finite elements for three-dimensional high-frequency problems," *IEEE Trans. Magn.*, vol. 34, no. 5, pp. 3288–3291, Sept. 1998.
- [6] R. N. Rieben, G. H. Rodrigue, and D. A. White, "A high-order mixed vector finite element method for solving the time dependent Maxwell equations on unstructured grids," *J. Comp. Phys.*, vol. 204, pp. 490–519, 2005.
- [7] B. He and F. L. Teixeira, "A sparse and explicit FETD via approximate inverse Hodge (mass) matrix," *IEEE Microw. Wireless Comp. Lett.*, vol. 16, no. 6, pp. 348–350, 2006.
- [8] R. A. Chilton and R. Lee, "The discrete origin of FETD-Newmark late-time instability, and a correction scheme," *J. Comp. Phys.*, vol. 224, no. 2, pp. 1293–1306, 2007.
- [9] B. Donderici and F. L. Teixeira, "Mixed finite-element time-domain method for Maxwell equations in doubly dispersive media," *IEEE Trans. Microwave Theory Tech.*, vol. 56, no. 1, pp. 113–120, 2008.
- [10] B. Donderici and F. L. Teixeira, "Conformal perfectly matched layer for the mixed finite-element time-domain method," *IEEE Trans. Antennas Propagat.*, vol. 56, no. 4, pp. 1017–1026, 2008.
- [11] N. M. Marais and D. B. Davidson, "Numerical evaluation of high-order finite element time domain formulations in electromagnetics," *IEEE Trans. Antennas Propagat.*, vol. 56, no. 12, pp. 3743–3751, Dec. 2008.
- [12] A. Taflov and S. Hagness *Computational Electrodynamics: The Finite Difference Time Domain, Third Edition* Boston, MA: Artech House, 2005.
- [13] B. He and F. L. Teixeira, "Differential forms, Galerkin duality, and sparse inverse approximations in finite element solutions of Maxwell equations," *IEEE Trans. Antennas Propagat.*, vol. 55, no. 5, pp. 1359–1368, May 2007.
- [14] M. J. Grote and T. Huckle, "Parallel preconditioning with sparse approximate inverses," *SIAM J. Sci. Comp.*, vol. 18, no. 3, pp.838–853, May 1997.
- [15] G.A. Deschamps, "Electromagnetics and differential forms," *Proc. IEEE*, vol. 69, no. 6, pp. 676–696, Jun. 1981.
- [16] A. Bossavit, "Whitney forms: a class of finite elements for three-dimensional computations in electromagnetism," *IEE Proc. Pt. A*, vol. 135, no. 8, pp. 493–500, Nov. 1988.
- [17] A. Bossavit, "'Generalized Finite Differences' in computational electromagnetics," in *Prog. Electromagnetics Research*, PIER 32 (F.L. Teixeira, ed.), pp. 45–64, EMW, 2001.
- [18] F. L. Teixeira, W.C. Chew, "Lattice electromagnetic theory from a topological viewpoint," *J. Math. Phys.*, vol. 40, pp. 169–187, Jan. 1999.
- [19] K. F. Warnick and D. V. Arnold, "Green forms for anisotropic, inhomogeneous media," *J. Electromagn. Waves Applicat.*, vol. 11, pp. 1145–1164, 1997.
- [20] P. R. Kotiuga, "Helicity functionals and metric invariance in three dimensions," *IEEE Trans. Magn.*, vol. 25, pp. 2813–2815, 1989.
- [21] F. L. Teixeira and W. C. Chew, "Differential forms, metrics, and the reflectionless absorption of electromagnetic waves," *J. Electromagn. Waves Applicat.*, vol. 13, no. 5, pp. 665–686, 1999.
- [22] B. He and F. L. Teixeira, "Geometric finite element discretization of Maxwell equations in primal and dual spaces," *Phys. Lett. A*, vol. 349, pp. 1–14, 2006.
- [23] B. He and F.L. Teixeira, "On the degree of freedom of lattice electrodynamics," *Phys. Lett. A*, vol. 336, pp. 1–6, 2005.
- [24] L. W. Tu, *An Introduction to Manifolds*, Springer-Verlag, 2008.
- [25] D. Martin, *Manifold Theory: An Introduction for Mathematical Physicists*, Horwood Publishing Ltd., West Sussex, England, 2002.
- [26] P. R. Kotiuga, "Analysis of finite element matrices arising from discretizations of helicity functionals," *J. Appl. Phys.*, vol. 67, pp. 5815–5817, 1990.
- [27] S. Wang and F. L. Teixeira, "Some remarks on the stability of time-domain electromagnetic simulations," *IEEE Trans. Antennas Propagat.*, vol. 52, no. 3, pp. 895–898, 2004.
- [28] S. D. Gedney and J. A. Roden, "Numerical stability of non-orthogonal FDTD method," *IEEE Trans. Antennas Propagat.*, vol. 48, no.2, pp. 231–239, Feb. 2000.
- [29] A. Bondeson, T. Rylander, P. Ingelström, *Computational Electromagnetics*, Springer-Verlag, 2005.
- [30] Z. Jia and B. Zhu, "A power sparse approximate inverse preconditioning procedure for large sparse linear systems," *Numer. Linear Algebra Appl.*, vol. 16, pp. 259–299, 2009.
- [31] G. Allean, M. Benzi, and L. Giraud "Sparse approximate inverse preconditioning for dense linear systems arising in computational electromagnetics," *Numer. Algorithms*, vol. 16 pp. 115, 1997.
- [32] E. Chow, "A priori sparsity patterns for parallel sparse approximate inverse preconditioners," *SIAM J. Sci. Comput.*, vol. 21, pp. 1804–1822, 2000.